High Power Laser Science and Engineering, (2024), Vol. 12, e42, 7 pages.
doi:10.1017/hpl.2024.23

HIGH POWER LASER SCIENCE AND ENGINEERING

RESEARCH ARTICLE

Precise mode control of mid-infrared high-power laser diodes using on-chip advanced sawtooth waveguide designs

Jianmei Shi[1,2], Chengao Yang[1,2], Yihang Chen[1,2], Tianfang Wang[1,2], Hongguang Yu[1,2], Juntian Cao[1,2], Zhengqi Geng[1], Zhiyuan Wang[1], Haoran Wen[3], Hao Tan[3,4], Yu Zhang[1,2], Dongwei Jiang[1,2], Donghai Wu[1,2], Yingqiang Xu[1,2], Haiqiao Ni[1,2], and Zhichuan Niu[1,2]

[1] *Key Laboratory of Optoelectronic Materials and Devices, Institute of Semiconductors, Chinese Academy of Sciences, Beijing, China*

[2] *Center of Materials Science and Optoelectronics Engineering, University of Chinese Academy of Sciences, Beijing, China*

[3] *International Quantum Academy, Shenzhen, China*

[4] *Hefei National Laboratory, Hefei, China*

(Received 28 February 2024; revised 9 April 2024; accepted 23 April 2024)

Abstract

Power scaling in conventional broad-area (BA) lasers often leads to the operation of higher-order lateral modes, resulting in a multiple-lobe far-field profile with large divergence. Here, we report an advanced sawtooth waveguide (ASW) structure integrated onto a wide ridge waveguide. It strategically enhances the loss difference between higher-order modes and the fundamental mode, thereby facilitating high-power narrow-beam emission. Both optical simulations and experimental results illustrate the significant increase in additional scattering loss of the higher-order modes. The optimized ASW lasers achieve an impressive output power of 1.1 W at 4.6 A at room temperature, accompanied by a minimal full width at half maximum lateral divergence angle of 4.91°. Notably, the far-field divergence is reduced from 19.61° to 11.39° at the saturation current, showcasing a remarkable 42% improvement compared to conventional BA lasers. Moreover, the current dependence of divergence has been effectively improved by 38%, further confirming the consistent and effective lateral mode control capability offered by our design.

Keywords: antimonide semiconductor lasers; far-field; mode control

1. Introduction

High-power and high-beam-quality antimonide semiconductor diode lasers operating around 2 μm atmospheric transmission windows show considerable promise for industrial and medical applications as important and reliable light sources, such as high-sensitivity optical gas detection[1,2], spectroscopy[3,4], free space communication[5] and pumping solid-state lasers or fiber lasers[6].

Broad-area (BA) diode lasers[7], the most common commercially available diode type, hold paramount importance owing to their high output power and uncomplicated manufacturing process. However, affected by intrinsic physical mechanisms, such as thermal lensing induced by self-heating[8], lateral carrier accumulation at the ridge edge[9] and filamentation[10], the output beam exhibits large divergence and severe far-field expansion along the lateral direction at high injection currents. This drawback increases module complexity and size, hindering some potential breakthroughs of this device in critical application fields.

In fact, the laser lateral beam quality is determined by the state of the lateral modes present in the cavity. In the realm of high-power lasers, the mastery of lateral mode control has emerged as a pivotal technological advancement. A variety of approaches to control the lateral modes for low lateral far-field divergence and high-power output semiconductor lasers have been developed, such as photonic crystal spatial filtering[11], a phase controller[12,13] and an angled cavity[14,15]. However, most of them offer limited improvements in the sensitivity of lateral divergence to the injection current, and struggle to significantly enhance lateral far-field performance without noticeable compromises on output power. Moreover, certain methods are technologically intricate, consequently constraining their applicability. Microstructures[16–18] have been implemented in near- and mid-infrared lasers to

Correspondence to: C. Yang and Z. Niu, Key Laboratory of Optoelectronic Materials and Devices, Institute of Semiconductors, Chinese Academy of Sciences, Beijing 100083, China. Emails: yangchengao@semi.ac.cn (C. Yang); zcniu@semi.ac.cn (Z. Niu)

compensate for the poor mode discrimination of BA lasers by selectively introducing higher-order mode optical losses. Considering the power maintenance, simplicity and stable mode selection performance, the devices have great potential for applications.

In this paper, we report a low-divergence, high-power antimonide semiconductor laser with an advanced sawtooth waveguide (ASW) structure. The optical field simulation of the laser cavity demonstrates a significant mode filtering effect, which is well validated by a comprehensive characterization of the device. The ASW lasers exhibit a maximum continuous wave (CW) output power of 1.1 W at room temperature, a performance nearly identical to conventional lasers with the same output aperture. Notably, they deliver an approximate 42% improvement in lateral far-field divergence for a single emitter operating at watt-level power output compared to conventional BA lasers. In addition, the current dependence of the lateral divergence has been significantly improved by 38%. Furthermore, the device fabrication is compatible with the conventional BA laser process. It is worth emphasizing that the ASW structure significantly improves the far-field blooming effect, providing stable mode control capabilities in the whole power range. Such a structure allows superior power characteristics and a more uniform near-field, and enables more concentrated and narrower beam emission. These features, scalable to higher brightness operations, position it as an excellent candidate among numerous microstructure designs for highly integrated high-brightness laser systems.

2. Device design and fabrication

2.1. Sample fabrication

Figure 1(a) shows a schematic diagram of the ASW lasers. The designed isosceles triangles with 32 μm long equal sides have been introduced at a period of 42.5 μm. Figure 1(b) shows a scanning electron microscope (SEM) image of the

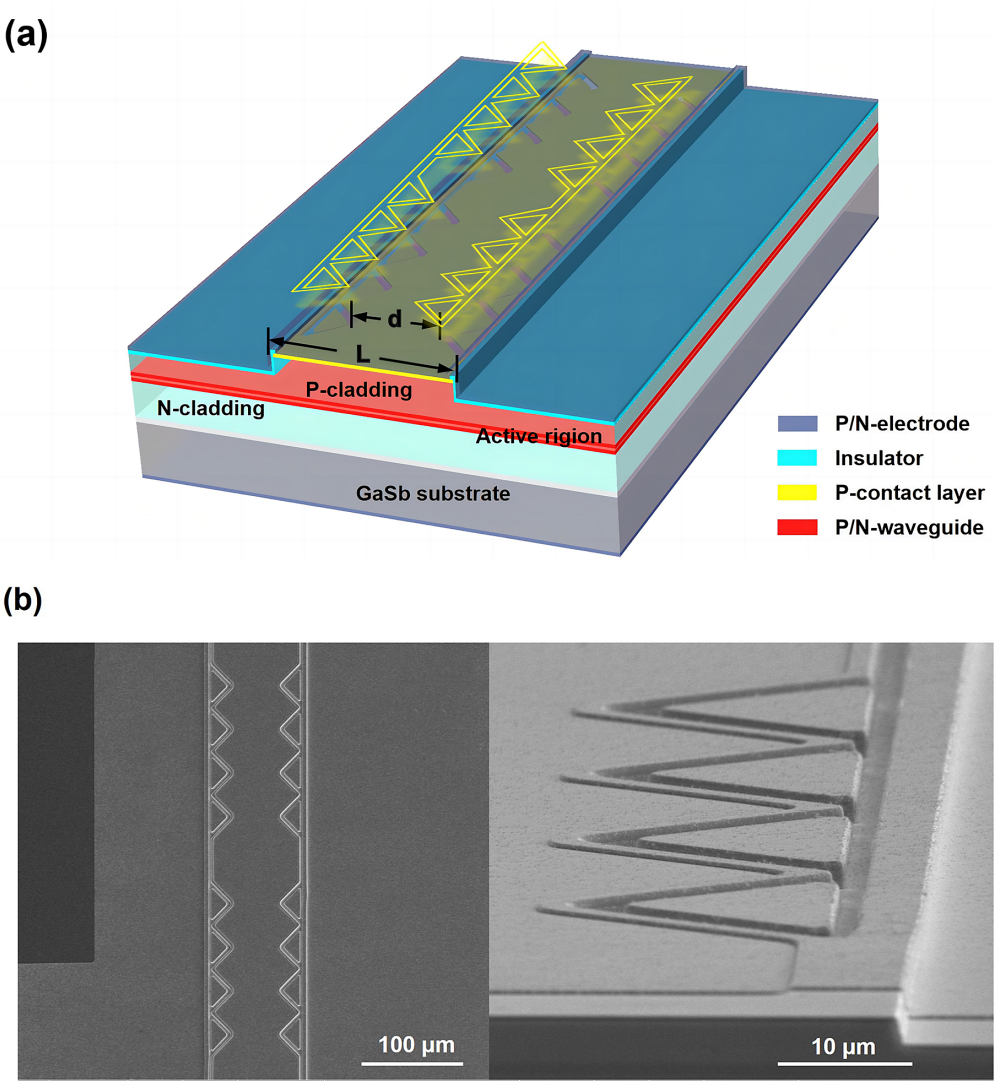

Figure 1. (a) Schematic diagram of the ASW lasers. (b) Scanning electron microscope image of the ASW lasers, top view (left) and enlarged view (right).

ASW lasers. The wafer was grown on an n-doped GaSb substrate by Veeco solid-source Gen-II molecular beam epitaxy (MBE). The active region presented in this work contained two compressively strained 10 nm thick $In_{0.18}GaSb$ quantum wells separated by a 20 nm $Al_{0.25}GaAs_{0.02}Sb$ barrier layer and two undoped 270 nm thick $Al_{0.25}GaAs_{0.02}Sb$ separate confinement layers. The top and bottom were 2 μm thick p-doped and n-doped $Al_{0.5}GaAs_{0.04}Sb$ cladding layers, respectively. The total thickness of the epitaxy layers was about 5 μm, including a 250 nm thick p^+ GaSb layer grown on the P-cladding layer and a 360 nm thick GaSb buffer grown on the substrate. After epitaxial growth, the ASW structure and ridge were formed through standard photolithography and an inductively coupled plasma (ICP) dry etching process from the same batch, with an etching depth of 2 μm. After depositing a 250 nm thick SiO_2 insulating layer via plasma-enhanced chemical vapor deposition (PECVD), electrode windows were created on the center of the ridge. Electrode layers consisting of Ti/Pt/Au and AuGe/Ni/Au were sputtered on the p-type and n-type sides, respectively, subsequent to reducing the wafer thickness to 125 μm. The lasers were coated with anti-reflection and high-reflection coatings. The reflectance of the ends of the lasers was 5% and 95%, respectively. Both ASW lasers and BA lasers were cleaved to a length of 1.5 mm and a width of 500 μm, mounted p-side down on C-mount copper heat sinks for better heat dissipation. All devices have the same emission aperture of 100 μm.

2.2. *Methods and simulation*

The optical field distribution of ASW lasers was simulated using the 2D finite difference time domain (FDTD) method. For the simulation, the input parameters were set to the experimental laser parameters, including the epitaxial structure, etching depth and microstructure size. The specific details of the ASW structure are shown in Figure 2. Figure 3 illustrates the calculated optical field distributions of lateral modes through the ASW structure for mode orders m = 0, 1, 2, 3, 6 and 8. As anticipated from the design of the ASW structure based on the characteristics of the near-field mode distribution[19], high-order modes experience noticeable increased scattering losses at the edges of the ridge, while the transmission of the fundamental mode remains largely unaffected. Figure 4(a) shows the ratios R_u of the residual energy for different order modes transmitted after four-period microstructures with different size ratios $(L-d)/L$, where L is the width of the ridge and d is the width of the unetched central region, as depicted in Figure 1(a). Notably, the fundamental mode and higher-order modes exhibit a notable disparity in loss characteristics. As the microstructure size ratio varies from 0.4 to 0.6, there is a synchronous increase in losses in each order mode. To strike a balance between preserving as much energy as possible in the fundamental mode and ensuring high losses in the higher-order modes, a microstructure size ratio of 0.5 was selected for the experiment. At this ratio, the remaining energy in the fundamental mode is approximately 1.4 times that of the higher-order modes. Figures 4(b)–4(f) illustrate the optical field densities of the high-order modes (m = 0, 1, 3, 6 and 8) before and after microstructure tailoring. The majority of the energy of the fundamental mode is preserved, while the intensity of the higher-order modes significantly decreases on both sides. This indicates the enhanced competitiveness of the fundamental mode, thereby reducing the number of lateral higher-order modes as the operating current increases[16]. Such a selection mechanism for fundamental and high-order modes holds great promise in achieving both high-power and low lateral divergence simultaneously.

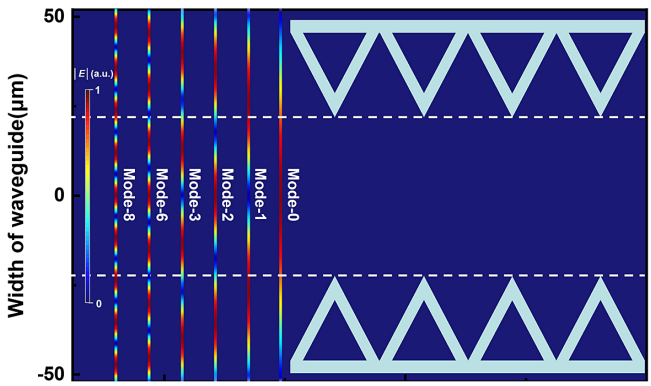

Figure 2. Details of the ASW structure. The inset shows the near-field distribution of different order modes of conventional BA lasers.

3. Results and discussion

Figure 5(a) shows the CW light power versus current (L–I) characteristics of the conventional BA lasers and ASW lasers at 288 K, with different periods and positions of microstructures. To validate the superiority of the waveguide design and derive further optimization strategies, a total of four sets of devices were fabricated. Specifically, lasers with eight-period microstructures distributed on both sides or gathered in the middle of the cavity are denoted as ASW-side and ASW-mid, respectively. In addition, lasers with microstructure covering the entire longitudinal direction and conventional BA lasers without microstructures are expressed as ASW and BA, respectively. The ASW-side, ASW-mid and BA structure have similar peak powers of about 1.1 W and slope efficiencies of 0.29 W/A. The maintenance of the output power may be explained by reduced mode competition and better matching of the lateral gain profile to the mode profile[20–23]. The ASW structure exhibits two regimes in slope efficiency of 0.27 and 0.16 W/A below and above 2.6 A, respectively, with an output power of 0.98 W at 4.6 A. This observation can be attributed to the substantial increase

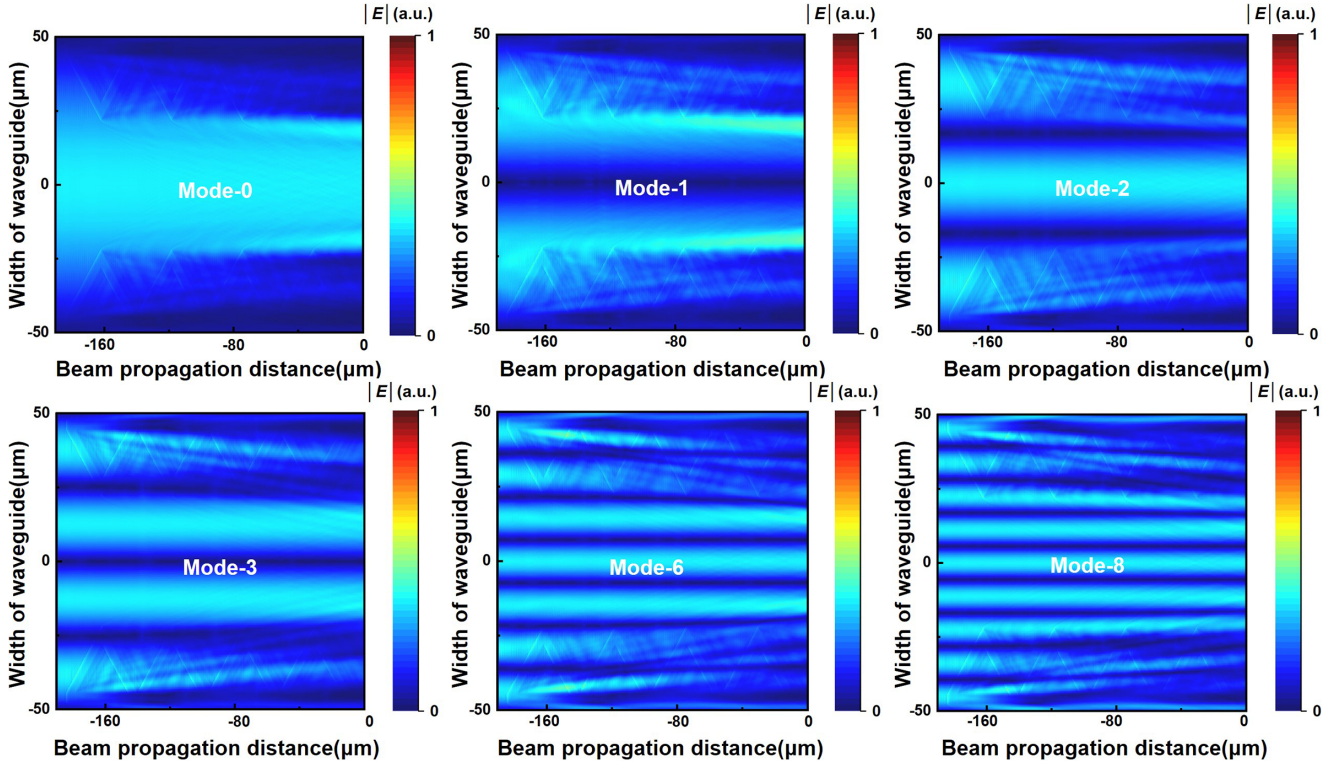

Figure 3. The optical field distributions of lateral modes with order numbers $m = 0$, 1, 2, 3, 6 and 8 through the ASW lasers, respectively.

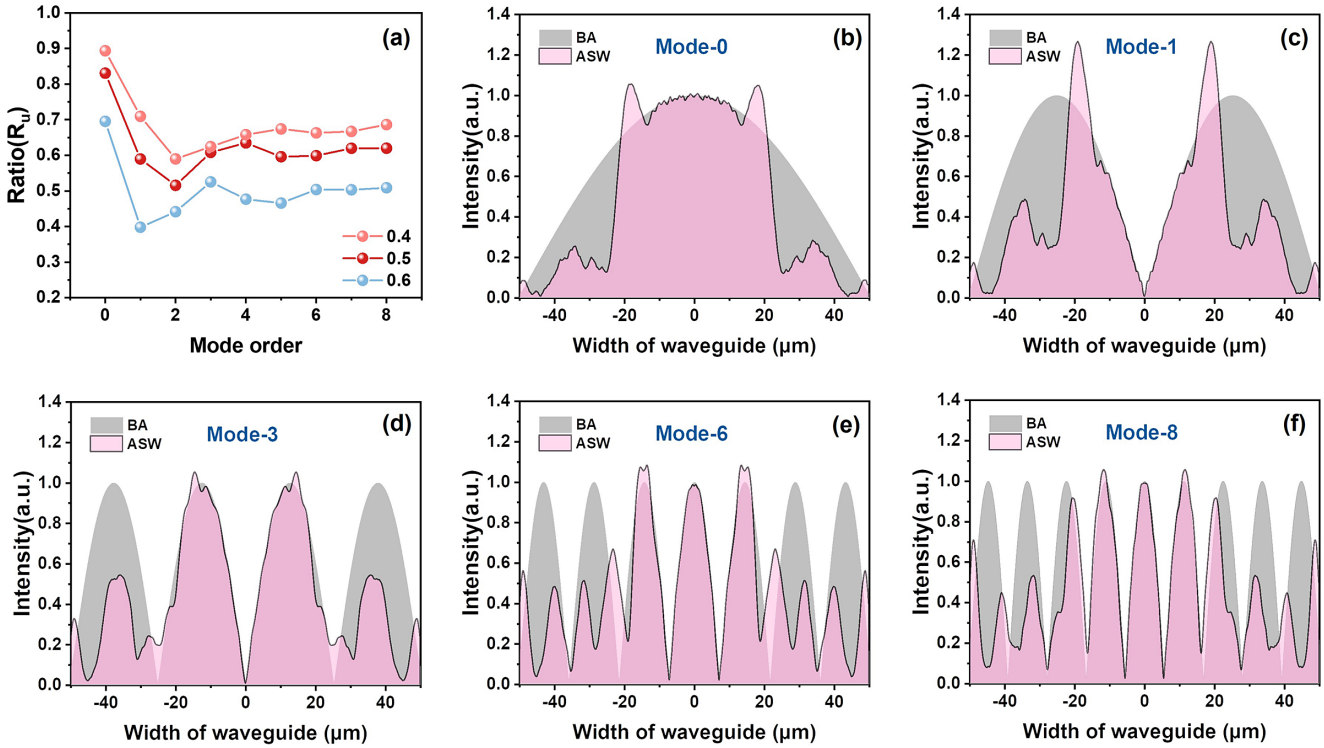

Figure 4. (a) Energy retained after transmitting different lateral modes through the ASW structure with microstructure size ratios of 0.4, 0.5 and 0.6. (b)–(f) Simulated optical field distribution of modes with order numbers $m = 0$, 1, 3, 6 and 8 at the facet of conventional BA lasers and ASW lasers with the microstructure size ratio of 0.5.

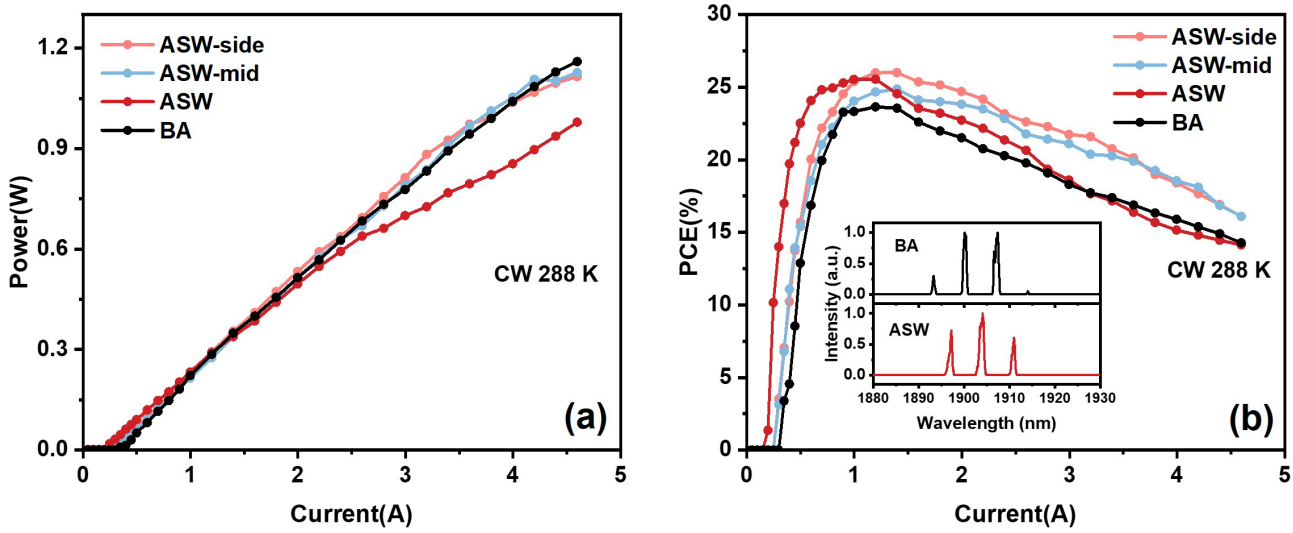

Figure 5. (a) *L–I* curves and (b) PCE–*I* curves of conventional BA lasers and ASW lasers with different positions and periods. The inset displays the spectra at 4.5 A of the BA laser and the ASW laser, respectively.

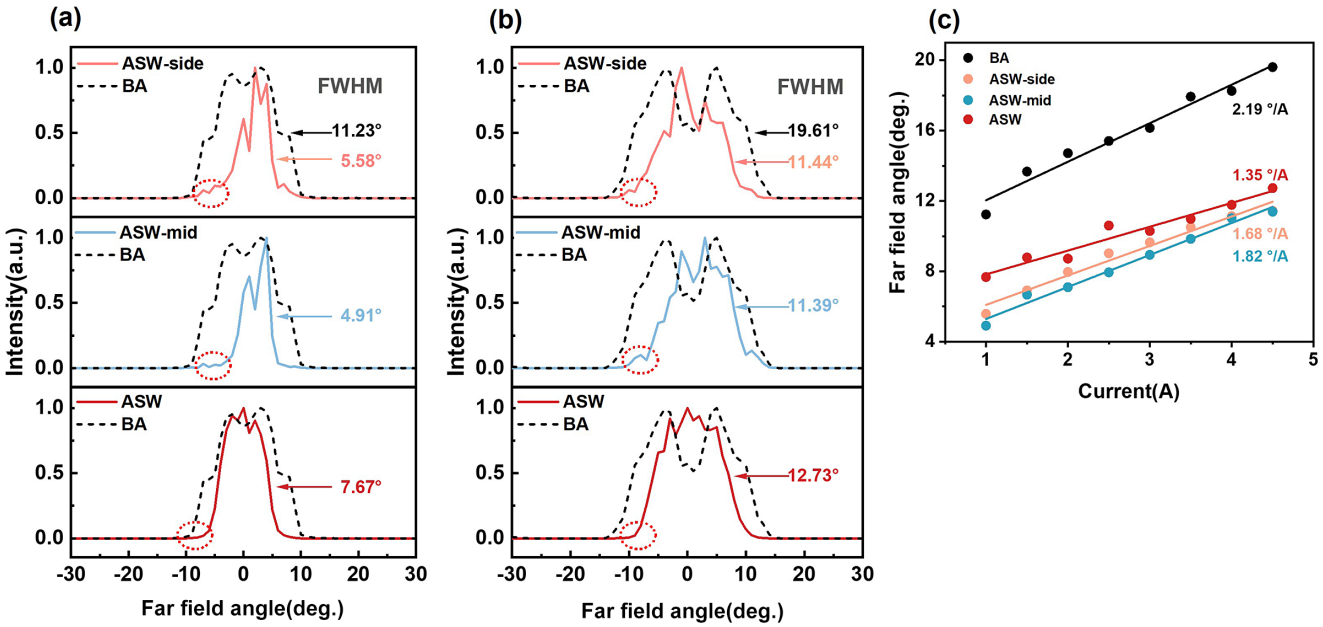

Figure 6. The lateral far-field profiles at (a) 1 A and (b) 4.5 A of conventional BA lasers and ASW lasers, respectively. (c) The lateral far-field angles depending on the injection current at 288 K of conventional BA lasers and ASW lasers.

in losses to higher-order modes compared to other devices, along with the sustained strong modulation effect of the proposed structure at high current levels. As the number of microstructure periods increases, there is a sequential decrease in the threshold current. Compared to conventional BA lasers, the threshold current of the ASW structure decreases from 0.35 to 0.20 A. This favorable outcome can be attributed to the dual suppression of lateral carrier accumulation effects[24,25], leading to an increase in effective injection efficiency. The power conversion efficiencies versus current (PCE–*I*) characteristics for conventional BA lasers and ASW lasers are shown in Figure 5(b). Clearly, in comparison to the conventional BA laser, both the ASW-side structure and ASW-mid structure exhibit higher PCE across the whole power range. The maximum PCE for the ASW structure is 25.5%, surpassing the 23.6% of the conventional BA laser. At elevated current levels, these two values tend to converge, reaching 14% at 4.6 A. The inset depicts the spectra recorded at 4.5 A for the BA laser and the ASW laser. The central emission wavelength for both devices is in the 1900 nm region.

Our design, on the other hand, shows a much improved far-field performance. The lateral far-field profiles of the above devices under CW operation at 1 and 4.5 A at a heat

sink temperature of 288 K were measured and are shown in Figures 6(a) and 6(b), respectively. The conventional BA laser exhibits a typical double-lobe feature, whereas all the ASW lasers demonstrate narrower and more concentrated far-field profiles. The far-field profiles of the ASW-side structure and ASW-mid structure closely resemble each other. The lateral far-field angle of the ASW-mid structure increases from 4.91° to 11.39° full width at half maximum (FWHM) with increasing drive current from 1 to 4.5 A. This represents a reduction of 56% and 42% compared to the conventional BA laser, which has angles of 11.23° and 19.61° at these respective currents. The broadening is a consequence of the enhanced index guiding in the lateral dimension resulting from self-heating[26]. The ASW structure has slightly larger lateral divergence compared to the ASW-side structure and ASW-mid structure, producing 7.67° and 12.73° divergence at a drive current of 1 and 4.5 A, respectively. However, it is worth noting that the advantage of the ASW structure lies in significantly reducing certain minor side lobes, as indicated by the red dashed circles. This further confirms the effective suppression of higher-order modes by the proposed structure, which is consistent with near-field simulation results. Figure 6(c) displays the lateral far-field divergence angle as a function of injection current, ranging from 1 to 4.5 A. Notably, all the ASW lasers exhibit smaller lateral divergence compared to the conventional BA laser in the whole dynamic current range. The divergence angles of the ASW-side structure and ASW-mid structure gradually increase with current-dependent values of 1.68 and 1.82 deg/A, respectively. The ASW structure has the lowest current dependence at 1.35 deg/A, achieving a 38% improvement compared to the 2.19 deg/A observed in BA lasers. This indicates a significant enhancement in the lateral far-field blooming effect[27]. Furthermore, it is evident that for this device, the variations in the position of the microstructure along the longitudinal direction of the cavity have a minor impact on output power and lateral far-field performance. To enhance device performance, simulation and experimental projects will be further improved for better alignment between mode profiles and carrier density profiles[19,21].

4. Conclusion

In summary, we presented a waveguide structure designed for high-power antimonide semiconductor lasers. This design mitigates the unfavorable far-field characteristics typically associated with BA lasers while preserving their advantages. The approach involves enhancing the scattering loss of higher-order lateral modes by incorporating sawtooth structures along the longitudinal direction of the ridges. The influence of these ASW designs was experimentally evaluated, in conjunction with laser diodes fabricated with optimized waveguide parameters. The resulting ASW lasers generated a total optical output power of 1.1 W in CW mode at 288 K, with a minimum lateral FWHM beam divergence angle of 4.91°. Importantly, they maintained excellent suppression of higher-order modes across the whole current range, showcasing remarkable lateral divergence characteristics with a current dependence of 1.35 deg/A. These attributes, marked by their narrow-beam divergence and high-power output, enable compact high-brightness laser systems to be utilized across a wider range of application scenarios.

Acknowledgement

The work was supported by the National Natural Science Foundation of China (Grant No. 62204238); the Innovation Program for Quantum Science and Technology (Grant No. 2021ZD0300801); ‘Announce the list and take charge’ of the Major Special Plan of Science and Technology in Shanxi Province (Grant No. 202201030201009); and the National Key R&D Program of China (Grant No. 2019YFA0705203).

References

1. Q. Gaimard, M. Triki, T. Nguyen-Ba, L. Cerutti, G. Boissier, R. Teissier, A. Baranov, Y. Rouillard, and A. Vicet, Opt. Express **23**, 19118 (2015).
2. T. Milde, M. Hoppe, H. Tatenguem, M. Honsberg, M. Mordmueller, J. O’Gorman, W. Schade, and J. Sacher, Proc. SPIE **10553**, 105530C (2018).
3. L. Dong, F. K. Tittel, C. Li, N. P. Sanchez, H. Wu, C. Zheng, Y. Yu, A. Sampaolo, and R. J. Griffin, Opt. Express **24**, A528 (2016).
4. J. Haas and B. Mizaikoff, Annu. Rev. Anal. Chem. **9**, 45 (2016).
5. P. Didier, H. Knoetig, O. Spitz, L. Cerutti, A. Lardschneider, E. Awwad, D. Diaz-Thomas, A. N. Baranov, R. Weih, J. Koeth, E. Schwarz, and F. Grillot, Photonics Res. **11**, 582 (2023).
6. G. L. Belenky, L. Shterengas, J. G. Kim, R. Martinelli, S. Suchalkin, and M. V. Kisin, Proc. SPIE **5732**, 169 (2005).
7. T. Hosoda, F. Tao, L. Shterengas, G. Kipshidze, and G. Belenky, Appl. Phys. Lett. **108**, 1089 (2016).
8. A. I. Bawamia, B. Eppich, K. Paschke, H. Wenzel, F. Schnieder, G. Erbert, and G. Traenkle, Appl. Phys. B **97**, 95 (2009).
9. M. Winterfeldt, P. Crump, S. Knigge, A. Maassdorf, U. Zeimer, and G. Erbert, IEEE Photonics Technol. Lett. **27**, 1809 (2015).
10. J. P. Leidner and J. R. Marciante, IEEE J. Quantum Electron. **50**, 267 (2014).
11. S. Gawali, D. Gailevicius, G. Garre-Werner, V. Purlys, C. Cojocaru, J. Trull, J. Montiel-Ponsoda, and K. Staliunas, Appl. Phys. Lett. **115**, 141104 (2019).
12. J. P. Hohimer, D. C. Craft, G. A. Vawter, and D. R. Myers, Appl. Phys. Lett. **58**, 2886 (1991).
13. H.-C. Eckstein, U. D. Zeitner, A. Tuennermann, W. Schmid, U. Strauss, and C. Lauer, Opt. Lett. **38**, 4480 (2013).
14. Z. Lu, L. Wang, Z. Zhao, S. Shu, G. Hou, H. Lu, S. Tian, C. Tong, and L. Wang, Chin. Opt. Lett. **15**, 081402 (2017).
15. D. Heydari, Y. Bai, N. Bandyopadhyay, S. Slivken, and M. Razeghi, Appl. Phys. Lett. **106**, 091105 (2015).
16. L. Wang, C. Tong, S. Shu, S. Tian, F. Sun, Y. Zhao, H. Lu, X. Zhang, G. Hou, and L. Wang, Opt. Lett. **44**, 3562 (2019).
17. J. Chang, C. Xiong, Q. Qi, S. Hao, S. Liu, and X. Ma, IEEE Photonics Technol. Lett. **35**, 862 (2023).

18. J. Su, C. Tong, L. Wang, Y. Wang, H. Lu, Z. Zhao, J. Wang, S. Tan, S. Shu, and L. Wang, Opt. Express **28**, 13131 (2020).
19. J. Piprek, Proc. SPIE **8619**, 861910 (2013).
20. R. J. Lang, A. G. Larsson, and J. G. Cody, IEEE J. Quantum Electron. **27**, 312 (1991).
21. P. Crump, P. Leisher, T. Matson, V. Anderson, D. Schulte, J. Bell, J. Farmer, M. DeVito, R. Martinsen, Y. K. Kim, K. D. Choquette, G. Erbert, and G. Traenkle, Appl. Phys. Lett. **92**, 131113 (2008).
22. J. A. Fan, M. A. Belkin, F. Capasso, S. P. Khanna, M. Lachab, A. G. Davies, and E. H. Linfield, Appl. Phys. Lett. **92**, 031106 (2008).
23. J. Shi, C. Yang, T. Wang, Y. Chen, H. Yu, Y. Zhang, D. Wu, Y. Xu, H. Ni, and Z. Niu, Appl. Phys. Lett. **123**, 121105 (2023).
24. J. Rieprich, M. Winterfeldt, R. Kernke, J. W. Tomm, and P. Crump, J. Appl. Phys. **123**, 125703 (2018).
25. J. Piprek and Z. M. S. Li, Appl. Phys. Lett. **102**, 221110 (2013).
26. M. S. Zediker, H. An, Y. Xiong, C.-L. J. Jiang, B. Schmidt, and G. Treusch, Proc. SPIE **8965**, 89650U (2014).
27. T. Wang, L. Wang, S. Shu, S. Tian, Z. Zhao, C. Tong, and L. Wang, Chin. Opt. Lett. **15**, 071404 (2017).